

Low-mass vector-meson production at forward rapidity in $p+p$ and Au+Au collisions at $\sqrt{s_{NN}} = 200$ GeV

N.J. Abdulameer,^{15,22} U. Acharya,¹⁹ A. Adare,¹² C. Aidala,⁴² N.N. Ajitanand,^{60,*} Y. Akiba,^{55,56,†}
M. Alfred,²¹ D. Anderson,²⁷ V. Andrieux,⁴² S. Antsupov,⁵⁸ N. Apadula,^{27,61} H. Asano,^{34,55} B. Azmoun,⁷
V. Babintsev,²³ M. Bai,⁶ N.S. Bandara,⁴⁰ B. Bannier,⁶¹ E. Bannikov,⁵⁸ K.N. Barish,⁸ S. Bathe,^{5,56}
A. Bazilevsky,⁷ M. Beaumier,⁸ S. Beckman,¹² R. Belmont,^{12,49} A. Berdnikov,⁵⁸ Y. Berdnikov,⁵⁸ L. Bichon,⁶⁶
B. Blankenship,⁶⁶ D.S. Blau,^{33,46} J.S. Bok,⁴⁸ V. Borisov,⁵⁸ K. Boyle,⁵⁶ M.L. Brooks,³⁶ J. Bryslawskyj,^{5,8}
V. Bumazhnov,²³ S. Campbell,^{13,27} R. Cervantes,⁶¹ P. Chaitanya,⁶¹ C.-H. Chen,⁵⁶ D. Chen,⁶¹ M. Chiu,⁷
C.Y. Chi,¹³ I.J. Choi,²⁴ J.B. Choi,^{29,*} T. Chujo,⁶⁴ Z. Citron,⁶⁷ M. Connors,^{19,56} R. Corliss,⁶¹ N. Cronin,^{44,61}
M. Csanád,¹⁶ T. Csörgő,^{41,68} T.W. Danley,⁵⁰ A. Datta,⁴⁷ M.S. Daugherty,¹ G. David,^{7,61} K. DeBlasio,⁴⁷
K. Dehmelt,⁶¹ A. Denisov,²³ A. Deshpande,^{56,61} E.J. Desmond,⁷ A. Dion,⁶¹ P.B. Diss,³⁹ D. Dixit,⁶¹ V. Doomra,⁶¹
J.H. Do,⁶⁹ A. Drees,⁶¹ K.A. Drees,⁶ J.M. Durham,³⁶ A. Durum,²³ H. En'yo,⁵⁵ A. Enokizono,^{55,57} R. Esha,⁶¹
B. Fadem,⁴⁴ W. Fan,⁶¹ N. Feege,⁶¹ D.E. Fields,⁴⁷ M. Finger, Jr.,⁹ M. Finger,⁹ D. Firak,^{15,61} D. Fitzgerald,⁴²
S.L. Fokin,³³ J.E. Frantz,⁵⁰ A. Franz,⁷ A.D. Frawley,¹⁸ Y. Fukuda,⁶⁴ P. Gallus,¹⁴ C. Gal,⁶¹ P. Garg,^{3,61} H. Ge,⁶¹
F. Giordano,²⁴ A. Glenn,³⁵ Y. Goto,^{55,56} N. Grau,² S.V. Greene,⁶⁶ M. Grosse Perdekamp,²⁴ T. Gunji,¹¹
T. Guo,⁶¹ H. Guragain,¹⁹ T. Hachiya,^{55,56} J.S. Haggerty,⁷ K.I. Hahn,¹⁷ H. Hamagaki,¹¹ H.F. Hamilton,¹
J. Hanks,⁶¹ S.Y. Han,^{17,32} S. Hasegawa,²⁸ T.O.S. Haseler,¹⁹ K. Hashimoto,^{55,57} T.K. Hemmick,⁶¹ X. He,¹⁹
J.C. Hill,²⁷ K. Hill,¹² A. Hodges,^{19,24} R.S. Hollis,⁸ K. Homma,²⁰ B. Hong,³² T. Hoshino,²⁰ N. Hotvedt,²⁷
J. Huang,⁷ K. Imai,²⁸ M. Inaba,⁶⁴ A. Iordanova,⁸ D. Isenhower,¹ D. Ivanishchev,⁵⁴ B.V. Jacak,⁶¹ M. Jezghani,¹⁹
X. Jiang,³⁶ Z. Ji,⁶¹ B.M. Johnson,^{7,19} D. Jouan,⁵² D.S. Jumper,²⁴ S. Kanda,¹¹ J.H. Kang,⁶⁹ D. Kapukchyan,⁸
S. Karthas,⁶¹ G. Kasza,^{41,68} D. Kawall,⁴⁰ A.V. Kazantsev,³³ J.A. Key,⁴⁷ V. Khachatryan,⁶¹ A. Khanzadeev,⁵⁴
B. Kimelman,⁴⁴ C. Kim,^{8,32} D.J. Kim,³⁰ E.-J. Kim,²⁹ G.W. Kim,¹⁷ M. Kim,⁵⁹ D. Kincses,¹⁶ E. Kistenev,⁷
R. Kitamura,¹¹ J. Klatsky,¹⁸ D. Kleinjan,⁸ P. Kline,⁶¹ T. Koblesky,¹² B. Komkov,⁵⁴ D. Kotov,^{54,58} L. Kovacs,¹⁶
S. Kudo,⁶⁴ K. Kurita,⁵⁷ M. Kurosawa,^{55,56} Y. Kwon,⁶⁹ J.G. Lajoie,^{27,51} D. Larionova,⁵⁸ A. Lebedev,²⁷ S. Lee,⁶⁹
S.H. Lee,^{27,61} M.J. Leitch,³⁶ Y.H. Leung,⁶¹ S.H. Lim,^{36,69} M.X. Liu,³⁶ X. Li,¹⁰ X. Li,³⁶ V.-R. Loggins,²⁴
D.A. Loomis,⁴² K. Lovasz,¹⁵ D. Lynch,⁷ S. Lökös,⁴¹ T. Majoros,¹⁵ Y.I. Makdisi,⁶ M. Makek,⁷⁰ A. Manion,⁶¹
V.I. Manko,³³ E. Mannel,⁷ M. McCumber,³⁶ P.L. McGaughey,³⁶ D. McGlinchey,^{12,36} C. McKinney,²⁴ A. Meles,⁴⁸
M. Mendoza,⁸ A.C. Mignerey,³⁹ A. Milov,⁶⁷ D.K. Mishra,⁴ J.T. Mitchell,⁷ M. Mitranskova,^{58,61} Iu. Mitrankov,^{58,61}
G. Mitsuka,^{31,56} S. Miyasaka,^{55,63} S. Mizuno,^{55,64} A.K. Mohanty,⁴ P. Montuenga,²⁴ T. Moon,^{32,69} D.P. Morrison,⁷
T.V. Moukhanova,³³ B. Mulilo,^{32,55,71} T. Murakami,^{34,55} J. Murata,^{55,57} A. Mwai,⁶⁰ K. Nagai,⁶³ K. Nagashima,²⁰
T. Nagashima,⁵⁷ J.L. Nagle,¹² M.I. Nagy,¹⁶ I. Nakagawa,^{55,56} H. Nakagomi,^{55,64} K. Nakano,^{55,63} C. Nattrass,⁶²
P.K. Netrakanti,⁴ T. Niida,⁶⁴ S. Nishimura,¹¹ R. Nouicer,^{7,56} N. Novitzky,^{30,61} T. Novák,^{41,68} G. Nukazuka,^{55,56}
A.S. Nyanin,³³ E. O'Brien,⁷ C.A. Ogilvie,²⁷ J.D. Orjuela Koop,¹² M. Orosz,^{15,22} J.D. Osborn,^{42,51} A. Oskarsson,³⁷
G.J. Ottino,⁴⁷ K. Ozawa,^{31,64} R. Pak,⁷ V. Pantuev,²⁵ V. Papavassiliou,⁴⁸ J.S. Park,⁵⁹ S. Park,^{43,55,59,61} M. Patel,²⁷
S.F. Pate,⁴⁸ J.-C. Peng,²⁴ D.V. Perepelitsa,^{7,12} G.D.N. Perera,⁴⁸ D.Yu. Peressounko,³³ C.E. PerezLara,⁶¹
J. Perry,²⁷ R. Petti,^{7,61} M. Phipps,^{7,24} C. Pinkenburg,⁷ R. Pinson,¹ R.P. Pisani,⁷ M. Potekhin,⁷ M.L. Purschke,⁷
J. Rak,³⁰ B.J. Ramson,⁴² I. Ravinovich,⁶⁷ K.F. Read,^{51,62} D. Reynolds,⁶⁰ V. Riabov,^{46,54} Y. Riabov,^{54,58}
D. Richford,^{5,65} T. Rinn,²⁷ S.D. Rolnick,⁸ M. Rosati,²⁷ Z. Rowan,⁵ J.G. Rubin,⁴² A.S. Safonov,⁵⁸ B. Sahlmueller,⁶¹
N. Saito,³¹ T. Sakaguchi,⁷ H. Sako,²⁸ V. Samsonov,^{46,54} M. Sarsour,¹⁹ S. Sato,²⁸ B. Schaefer,⁶⁶ B.K. Schmoll,⁶²
K. Sedgwick,⁸ R. Seidl,^{55,56} A. Seleznev,⁵⁸ A. Sen,^{27,62} R. Seto,⁸ P. Sett,⁴ A. Sexton,³⁹ D. Sharma,⁶¹ I. Shein,²³
T.-A. Shibata,^{55,63} K. Shigaki,²⁰ M. Shimomura,^{27,45} T. Shioya,⁶⁴ P. Shukla,⁴ A. Sickles,^{7,24} C.L. Silva,³⁶
D. Silvermyr,^{37,51} B.K. Singh,³ C.P. Singh,^{3,*} V. Singh,³ M. Slunečka,⁹ K.L. Smith,^{18,36} M. Snowball,³⁶
R.A. Soltz,³⁵ W.E. Sondheim,³⁶ S.P. Sorensen,⁶² I.V. Sourikova,⁷ P.W. Stankus,⁵¹ M. Stepanov,^{40,*}
S.P. Stoll,⁷ T. Sugitate,²⁰ A. Sukhanov,⁷ T. Sumita,⁵⁵ J. Sun,⁶¹ Z. Sun,^{15,22,61} J. Sziklai,⁶⁸ A. Taketani,^{55,56}
K. Tanida,^{28,56,59} M.J. Tannenbaum,⁷ S. Tarafdar,^{66,67} A. Taranenko,^{46,60} G. Tarnai,¹⁵ R. Tieulent,^{19,38}
A. Timilsina,²⁷ T. Todoroki,^{55,56,64} M. Tomášek,¹⁴ C.L. Towell,¹ R. Towell,¹ R.S. Towell,¹ I. Tserruya,⁶⁷
Y. Ueda,²⁰ B. Ujvari,^{15,22} H.W. van Hecke,³⁶ J. Velkovska,⁶⁶ M. Virius,¹⁴ V. Vrba,^{14,26} N. Vukman,⁷⁰
X.R. Wang,^{48,56} Y. Watanabe,^{55,56} Y.S. Watanabe,^{11,31} F. Wei,⁴⁸ A.S. White,⁴² C.L. Woody,⁷ M. Wysocki,⁵¹
B. Xia,⁵⁰ L. Xue,¹⁹ C. Xu,⁴⁸ Q. Xu,⁶⁶ S. Yalcin,⁶¹ Y.L. Yamaguchi,^{11,61} H. Yamamoto,⁶⁴ A. Yanovich,²³
I. Yoon,⁵⁹ J.H. Yoo,³² I.E. Yushmanov,³³ H. Yu,^{48,53} W.A. Zajc,¹³ A. Zelenski,⁶ S. Zhou,¹⁰ and L. Zou⁸

(PHENIX Collaboration)

[†]Abilene Christian University, Abilene, Texas 79699, USA

- ²Department of Physics, Augustana University, Sioux Falls, South Dakota 57197, USA
- ³Department of Physics, Banaras Hindu University, Varanasi 221005, India
- ⁴Bhabha Atomic Research Centre, Bombay 400 085, India
- ⁵Baruch College, City University of New York, New York, New York, 10010 USA
- ⁶Collider-Accelerator Department, Brookhaven National Laboratory, Upton, New York 11973-5000, USA
- ⁷Physics Department, Brookhaven National Laboratory, Upton, New York 11973-5000, USA
- ⁸University of California-Riverside, Riverside, California 92521, USA
- ⁹Charles University, Faculty of Mathematics and Physics, 180 00 Troja, Prague, Czech Republic
- ¹⁰Science and Technology on Nuclear Data Laboratory, China Institute of Atomic Energy, Beijing 102413, People's Republic of China
- ¹¹Center for Nuclear Study, Graduate School of Science, University of Tokyo, 7-3-1 Hongo, Bunkyo, Tokyo 113-0033, Japan
- ¹²University of Colorado, Boulder, Colorado 80309, USA
- ¹³Columbia University, New York, New York 10027 and Nevis Laboratories, Irvington, New York 10533, USA
- ¹⁴Czech Technical University, Zikova 4, 166 36 Prague 6, Czech Republic
- ¹⁵Debrecen University, H-4010 Debrecen, Egyetem tér 1, Hungary
- ¹⁶ELTE, Eötvös Loránd University, H-1117 Budapest, Pázmány P. s. 1/A, Hungary
- ¹⁷Ewha Womans University, Seoul 120-750, Korea
- ¹⁸Florida State University, Tallahassee, Florida 32306, USA
- ¹⁹Georgia State University, Atlanta, Georgia 30303, USA
- ²⁰Physics Program and International Institute for Sustainability with Knotted Chiral Meta Matter (WPI-SKCM2), Hiroshima University, Higashi-Hiroshima, Hiroshima 739-8526, Japan
- ²¹Department of Physics and Astronomy, Howard University, Washington, DC 20059, USA
- ²²HUN-REN ATOMKI, H-4026 Debrecen, Bem tér 18/c, Hungary
- ²³IHEP Protvino, State Research Center of Russian Federation, Institute for High Energy Physics, Protvino, 142281, Russia
- ²⁴University of Illinois at Urbana-Champaign, Urbana, Illinois 61801, USA
- ²⁵Institute for Nuclear Research of the Russian Academy of Sciences, prospekt 60-letiya Oktyabrya 7a, Moscow 117312, Russia
- ²⁶Institute of Physics, Academy of Sciences of the Czech Republic, Na Slovance 2, 182 21 Prague 8, Czech Republic
- ²⁷Iowa State University, Ames, Iowa 50011, USA
- ²⁸Advanced Science Research Center, Japan Atomic Energy Agency, 2-4 Shirakata Shirane, Tokai-mura, Naka-gun, Ibaraki-ken 319-1195, Japan
- ²⁹Jeonbuk National University, Jeonju, 54896, Korea
- ³⁰Helsinki Institute of Physics and University of Jyväskylä, P.O.Box 35, FI-40014 Jyväskylä, Finland
- ³¹KEK, High Energy Accelerator Research Organization, Tsukuba, Ibaraki 305-0801, Japan
- ³²Korea University, Seoul 02841, Korea
- ³³National Research Center "Kurchatov Institute", Moscow, 123098 Russia
- ³⁴Kyoto University, Kyoto 606-8502, Japan
- ³⁵Lawrence Livermore National Laboratory, Livermore, California 94550, USA
- ³⁶Los Alamos National Laboratory, Los Alamos, New Mexico 87545, USA
- ³⁷Department of Physics, Lund University, Box 118, SE-221 00 Lund, Sweden
- ³⁸IPNL, CNRS/IN2P3, Univ Lyon, Université Lyon 1, F-69622, Villeurbanne, France
- ³⁹University of Maryland, College Park, Maryland 20742, USA
- ⁴⁰Department of Physics, University of Massachusetts, Amherst, Massachusetts 01003-9337, USA
- ⁴¹MATE, Institute of Technology, Laboratory of Femtoscopy, Károly Róbert Campus, H-3200 Gyöngyös, Mátrai út 36, Hungary
- ⁴²Department of Physics, University of Michigan, Ann Arbor, Michigan 48109-1040, USA
- ⁴³Mississippi State University, Mississippi State, Mississippi 39762, USA
- ⁴⁴Muhlenberg College, Allentown, Pennsylvania 18104-5586, USA
- ⁴⁵Nara Women's University, Kita-uoya Nishi-machi Nara 630-8506, Japan
- ⁴⁶National Research Nuclear University, MEPhI, Moscow Engineering Physics Institute, Moscow, 115409, Russia
- ⁴⁷University of New Mexico, Albuquerque, New Mexico 87131, USA
- ⁴⁸New Mexico State University, Las Cruces, New Mexico 88003, USA
- ⁴⁹Physics and Astronomy Department, University of North Carolina at Greensboro, Greensboro, North Carolina 27412, USA
- ⁵⁰Department of Physics and Astronomy, Ohio University, Athens, Ohio 45701, USA
- ⁵¹Oak Ridge National Laboratory, Oak Ridge, Tennessee 37831, USA
- ⁵²IPN-Orsay, Univ. Paris-Sud, CNRS/IN2P3, Université Paris-Saclay, BP1, F-91406, Orsay, France
- ⁵³Peking University, Beijing 100871, People's Republic of China
- ⁵⁴PNPI, Petersburg Nuclear Physics Institute, Gatchina, Leningrad region, 188300, Russia
- ⁵⁵RIKEN Nishina Center for Accelerator-Based Science, Wako, Saitama 351-0198, Japan
- ⁵⁶RIKEN BNL Research Center, Brookhaven National Laboratory, Upton, New York 11973-5000, USA
- ⁵⁷Physics Department, Rikkyo University, 3-34-1 Nishi-Ikebukuro, Toshima, Tokyo 171-8501, Japan
- ⁵⁸Saint Petersburg State Polytechnic University, St. Petersburg, 195251 Russia
- ⁵⁹Department of Physics and Astronomy, Seoul National University, Seoul 151-742, Korea
- ⁶⁰Chemistry Department, Stony Brook University, SUNY, Stony Brook, New York 11794-3400, USA
- ⁶¹Department of Physics and Astronomy, Stony Brook University, SUNY, Stony Brook, New York 11794-3800, USA
- ⁶²University of Tennessee, Knoxville, Tennessee 37996, USA

⁶³Department of Physics, Tokyo Institute of Technology, Oh-okayama, Meguro, Tokyo 152-8551, Japan

⁶⁴Tomonaga Center for the History of the Universe, University of Tsukuba, Tsukuba, Ibaraki 305, Japan

⁶⁵United States Merchant Marine Academy, Kings Point, New York 11024, USA

⁶⁶Vanderbilt University, Nashville, Tennessee 37235, USA

⁶⁷Weizmann Institute, Rehovot 76100, Israel

⁶⁸Institute for Particle and Nuclear Physics, HUN-REN Wigner Research Centre for Physics, (HUN-REN Wigner RCP, RMI), H-1525 Budapest 114, POBox 49, Budapest, Hungary

⁶⁹Yonsei University, IPAP, Seoul 120-749, Korea

⁷⁰Department of Physics, Faculty of Science, University of Zagreb, Bijenička c. 32 HR-10002 Zagreb, Croatia

⁷¹Department of Physics, School of Natural Sciences, University of Zambia, Great East Road Campus, Box 32379, Lusaka, Zambia

(Dated: July 8, 2025)

The PHENIX experiment at the Relativistic Heavy Ion Collider has measured low-mass vector-meson ($\omega + \rho$ and ϕ) production through the dimuon decay channel at forward rapidity ($1.2 < |y| < 2.2$) in $p+p$ and Au+Au collisions at $\sqrt{s_{NN}} = 200$ GeV. The low-mass vector-meson yield and nuclear-modification factor were measured as a function of the average number of participating nucleons, $\langle N_{\text{part}} \rangle$, and the transverse momentum p_T . These results were compared with those obtained via the kaon decay channel in a similar p_T range at midrapidity. The nuclear-modification factors in both rapidity regions are consistent within the uncertainties. A comparison of the $\omega + \rho$ and J/ψ mesons reveals that the light and heavy flavors are consistently suppressed across both p_T and $\langle N_{\text{part}} \rangle$. In contrast, the ϕ meson displays a nuclear-modification factor consistent with unity, suggesting strangeness enhancement in the medium formed.

I. INTRODUCTION

The formation of quark-gluon plasma (QGP) has been confirmed through experiments at both the Relativistic Heavy Ion Collider (RHIC) [1–4] and the Large Hadron Collider (LHC) [5–8]. After the initial confirmation, one of the primary objectives in high-energy nuclear physics, including the PHENIX experiment, has been to measure and explore the properties of the QGP. Strangeness, in particular, serves as an excellent probe of the QGP because strange quarks are produced in the early stages of the collision, and their behavior provides valuable insights into the QGP properties and dynamics.

The QGP is expected to enhance the production of strange quarks due to the relatively large mass of the strange quark and the abundance of gluons at high energies [9–19]. Studying the strange quark production and its interactions in heavy-ion collisions aids in the exploration of the QGP properties and the mechanisms governing quark and gluon interactions within it. Strange hadrons, such as hyperons and strange mesons, are sensitive to the temperature and chemical potential of the QGP. Their yields and momentum distributions can be used to extract information about the temperature and chemical potential of the QGP, providing essential thermodynamic data [20, 21].

The ϕ meson, with its nearly pure bound state of strange (s) and anti-strange (\bar{s}) quarks, provides an ideal system for studying strangeness enhancement. It is the lightest nearly pure bound state of strange quarks ($s\bar{s}$) with a mass comparable to the mass of the lightest

baryons, such as the proton, and can be measured at PHENIX for $p_T > 2.5$ GeV/ c over a broad rapidity range. Due to its longer lifetime (42 fm/ c) [10], which is much longer than the QGP lifetime (5 fm/ c) [1], the ϕ meson is less influenced by late hadronic rescattering, thus reflecting the initial evolution of the system. As a pure $s\bar{s}$ state, the ϕ meson also places constraints on models describing parton energy loss and recombination in the QGP [22, 23]. Therefore, the properties of the ϕ meson are primarily governed by conditions in the early partonic phase, making it an ideal probe to investigate the properties of matter created in relativistic ion collisions.

The production at RHIC of low-mass vector mesons (LVMs), such as the ϕ , ω , and ρ mesons, offers important insights into QGP, especially when studied through their dimuon decay channel. Leptons are not affected by the strong color field within the QGP and can travel to the detectors with minimal interference. As a result, studying LVM production via their dimuon decay channel is an excellent way to explore evolution of the system. The ω meson, composed of light valence quarks similar to the π^0 but with a larger mass (782 MeV/ c^2) [24, 25], serves as an additional tool for systematically examining parton energy loss and hadron production mechanisms in these collisions. While the measurement of the ρ meson spectral function can provide insights into in-medium modifications of hadron properties near the quantum-chromodynamics phase boundary, which are related to chiral symmetry restoration [26–28], resolving the ρ meson (770 MeV/ c^2) [24] spectral function in the two-muon channel requires better mass resolution than the muon spectrometers of the PHENIX experiment can offer. Due to this limitation, the ρ meson cannot be distinguished from the ω meson, so the combined measurement of $\omega + \rho$ is typically reported.

Furthermore, measurements of the $\omega + \rho$ and ϕ

* Deceased

† PHENIX Spokesperson: akiba@rcf.rhic.bnl.gov

mesons, when combined with earlier J/ψ data [29] in the same kinematic region, offer a valuable opportunity to investigate the flavor dependence of medium effects. The $\omega + \rho$, ϕ , and J/ψ mesons comprise a closed system of light, strange, and charm quarks, respectively, and comparing the production of these mesons could provide insight into their respective interactions and behavior in the medium.

In this paper, the production of LVMs, $\omega + \rho$ and ϕ mesons, is determined, in $p+p$ and Au+Au collisions at $\sqrt{s_{NN}} = 200$ GeV in the forward and backward rapidity regions, using dimuons detected by the PHENIX muon spectrometers. The invariant yields of $\omega + \rho$ and ϕ mesons in $p+p$ collisions will serve as a baseline for the Au+Au measurements. Although the production in $p+p$ collisions was measured previously by PHENIX [30], changes in the detector setup between the Au+Au and $p+p$ data collections necessitate extracting the $p+p$ invariant yield from a more recent data set to account for any potential variations in systematic effects. Measurements of the LVM nuclear-modification factor (R_{AA}) as a function of p_T and the average number of participating nucleons are also presented. The results discussed are based on Au+Au collisions at $\sqrt{s_{NN}} = 200$ GeV recorded in 2014 with an integrated luminosity of 7.5 nb^{-1} , and $p+p$ collisions at $\sqrt{s} = 200$ GeV recorded in 2015 with an integrated luminosity of 47 pb^{-1} .

II. EXPERIMENTAL SETUP

A detailed description of the PHENIX detector is available in Ref. [31]. Here, we provide a brief overview of the detector subsystems relevant to these measurements. The key systems, depicted in Fig. 1, comprise forward silicon-vertex trackers (FVTX) [32], hadron absorbers, and muon spectrometers [33].

The FVTX is a silicon detector designed to accurately measure the collision vertex, with additional data provided by the silicon vertex tracker (VTX) at midrapidity. Together, the VTX and FVTX determine the radial distance of closest approach (DCA_R) by projecting the particle track from the FVTX onto a plane in the z -axis at the primary vertex, as identified by the VTX. Precise measurement of DCA_R enables a statistical separation of muons from short-lived particles, such as heavy-flavor mesons, and long-lived particles like pions and kaons, thereby significantly improving the signal-to-background ratio in the low mass region. The FVTX also provides precise tracking for charged particles entering the muon spectrometer before they undergo multiple scattering in the hadron absorber. Located downstream of the FVTX with respect to the interaction region, the hadron absorber comprises layers of copper, iron, and stainless steel, with a total thickness of 7.2 interaction lengths. It efficiently attenuates hadrons before they reach the muon arm, significantly reducing the hadronic background for muon-related measurements.

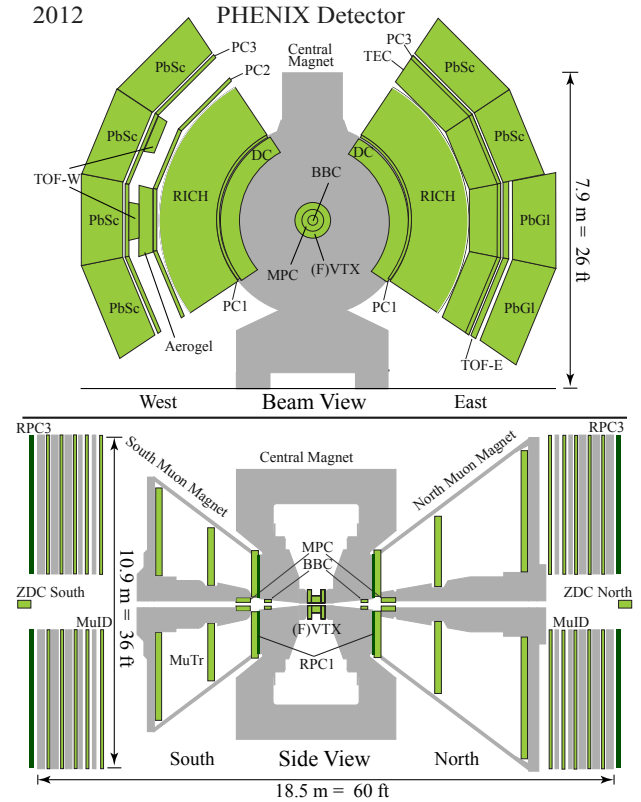


FIG. 1. A side view of the PHENIX detector, concentrating on the muon spectrometers instrumentation.

The absorber is followed by the muon spectrometer, which is composed of a muon tracker (MuTr) and a muon identifier (MuID). The MuTr, which is made up of three stations of cathode strip chambers placed within a magnet with a radial field integral of $0.72 \text{ T}\cdot\text{m}$. The MuID comprises five alternating layers of steel absorbers and Iarocci tubes. The overall momentum resolution, $\delta p/p$, for particles within the analyzed momentum range is $\approx 5\%$, independent of momentum, and is mainly constrained by multiple scattering.

In addition, two beam-beam counters (BBCs) are located on both sides of the interaction point and cover the pseudorapidity range $3.1 < |\eta| < 3.9$. These BBC detectors comprise 128 identical quartz photomultiplier tubes and function as a Čerenkov array. The BBC is used to measure the beam luminosity and form a minimum-bias (MB) trigger. It is also used to determine the vertex position along the direction of the beam and classify event centrality based on the total charge recorded in the BBC. To categorize centrality, a Monte Carlo Glauber model calculation is employed. The model takes inputs such as the inelastic nucleon-nucleon cross section and the nuclear charge density to simulate the probability of collision between nuclei based on the nucleon-nucleon inelastic cross section. The total charge detected by the BBC is used to define the centrality classes, and Glauber model

provides the mean number of binary (nucleon-nucleon) collisions, $\langle N_{\text{coll}} \rangle$, for each centrality range [34, 35].

III. DATA ANALYSIS

A. Dataset and quality cuts

This section provides the details of the LVM measurements in the dimuon decay channel. The Au+Au data set used here was collected in 2014 from Au+Au collisions at $\sqrt{s_{NN}} = 200$ GeV, using a MB trigger requiring at least two hits in each of the BBC detectors. The MB trigger captures $92 \pm 2\%$ of the total Au+Au inelastic cross section. The $p+p$ data set for this analysis was recorded in 2015 from $p+p$ collisions at $\sqrt{s} = 200$ GeV, using a MB trigger that required at least one hit in each of the BBC detectors. In addition, the MuID Level-1 dimuon trigger was applied, which required at least two tracks to penetrate through the MuID to its last layer.

Muons are identified by requiring that a detected particle penetrates several layers of absorber material in the MuID, which drastically reduces the hadron contribution although some hadrons may punch through. The particles that pass this threshold are then matched with the tracks reconstructed by the MuTr. The FVTX detector provides additional space points near the collision vertex before the particle begins its trajectory through the muon-arm absorbers, improving the mass resolution.

A set of selections is applied to the data to isolate high-quality muon candidates and enhance the signal-to-background ratio. Event selection requires the BBC collision z-vertex to be reconstructed within ± 10 cm from the center of the interaction region along the beam axis. MuTr tracks are matched to MuID tracks at the first MuID layer in both position and angle, and only dimuon candidates in which both tracks penetrate the final MuID layer are considered. Furthermore, the track must have a minimum number of possible hits in both MuTr and MuID, and a maximum allowed χ^2 is applied to both the track and vertex determination. A minimum single-muon momentum along the beam axis, p_z , is required, which is reconstructed and energy loss corrected at the collision vertex. Furthermore, MuTr + MuID tracks are matched with FVTX tracks and a strict cut on DCA_R is applied. Finally, this analysis is restricted to the dimuon rapidity region of $1.2 < |y| < 2.2$ and p_T range of 2.5–5.0 GeV/ c . The p_T limitation is due to the large background and limited acceptance at low p_T and low statistics at high p_T .

B. Detector acceptance and reconstruction efficiency

The acceptance and reconstruction efficiency ($A\epsilon$) is determined using Monte Carlo (MC) simulation. The $A\epsilon$ is defined by the number of dimuons reconstructed in the

muon spectrometers relative to the number of dimuons generated in the same kinematic region. The kinematic distributions of PYTHIA¹ [36] generated p_T , rapidity, and LVM mass shape were used as input into a full PHENIX GEANT4 simulation [37]. The p_T , rapidity and vertex distributions were tuned such that the reconstructed distributions match those of the data. Variations within the uncertainties of the data are taken as systematic uncertainty.

The detector response in the simulation is tuned to a set of characteristics (dead and hot channel maps, gains, noise, etc.) that describes the performance of each detector subsystem. The simulated events are further embedded with real data to account for the effects of detector occupancy, noise and fake tracks, and then reconstructed in the same manner as the real data. As a cross-check, the calculated J/ψ invariant yield, after applying the $A\epsilon$ correction, showed good agreement with the published result [29] within the statistical uncertainties across all p_T and centrality bins.

Figure 2 shows the $A\epsilon$ of dimuon pairs as a function of (a) p_T , (b) centrality (%) for the forward (north) and backward (south) rapidities, covering the rapidity ranges $1.2 < y < 2.2$ and $-2.2 < y < -1.2$, respectively. The relative difference in $A\epsilon$ between the two spectrometers is due to the different detection efficiencies of the MuTr and MuID systems and different amounts of absorber material.

C. Raw yield extraction

The invariant mass distribution is constructed by combining muon candidate tracks of opposite charge. In the mass range $0.3 < m_{\mu\mu} < 2.5$ GeV/ c^2 , this unlike-sign invariant mass spectrum includes ϕ , ρ , and ω mesons, as well as uncorrelated and correlated backgrounds. The uncorrelated backgrounds arise from random combinatorial associations of muon candidates, while the correlated backgrounds result from the following processes: open charm decay (e.g., $D\bar{D}$ pairs where both decay semileptonically to muons), open beauty decay, η meson and ω meson Dalitz decays, or the Drell-Yan process.

The uncorrelated combinatorial background is addressed using two distinct methods: (1) like-sign dimuons and (2) event mixing. The like-sign dimuon background is constructed by pairing muon candidate tracks of the same charge, and is used to model the uncorrelated background under the assumption that like-sign dimuon pairs arise purely from combinatorial processes, with no correlation between single muons. In the event-mixing approach, muons from different events are randomly paired

¹ We used PYTHIA6 (ver 6.421), with parton distribution functions given by CTEQ6LL. The following parameters were modified: MSEL = 0, MSUB(86) = 1, PARP(91) = 2.1, MSTP(51) = 10041, MDME(858,1) = 0, MDME(859,1) = 1, MDME(860,1) = 0, and Tune A.

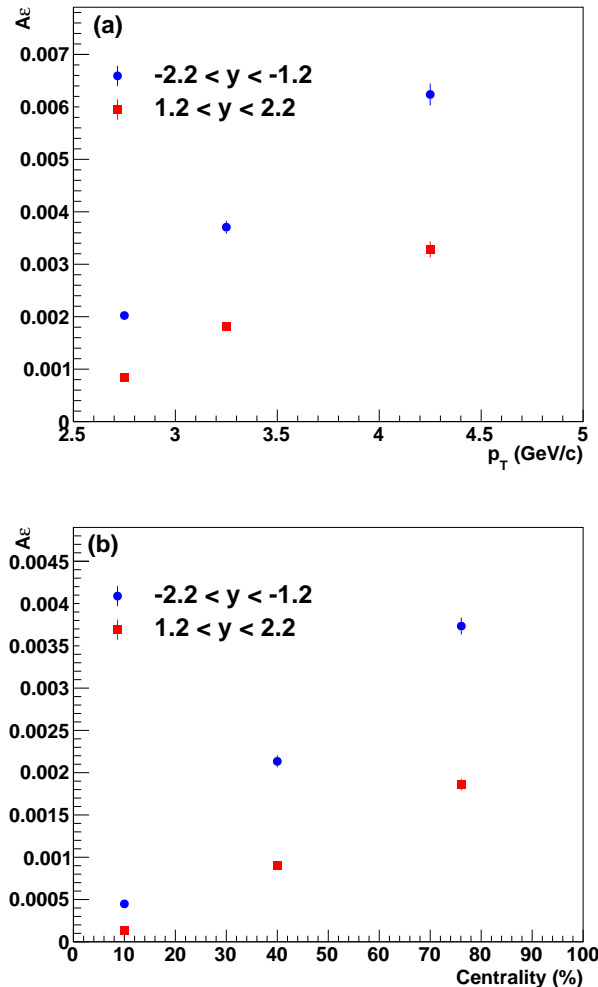


FIG. 2. $A\varepsilon$ of dimuon pairs in Au+Au collisions as a function of (a) p_T , (b) centrality.

to generate a background distribution of uncorrelated dimuon pairs. Events are mixed with four previous events within the same 2% centrality and 1-cm z-vertex bins to minimize systematic uncertainties. Detailed descriptions of both techniques can be found in Ref. [38]. Although the uncorrelated background distributions were consistent between the two methods, the event-mixing technique is employed in this analysis due to the statistical limitations of the like-sign method.

To extract the LVM signal, the unlike-sign invariant mass spectrum is fitted with a combination of two Gaussian functions, a Breit-Wigner function convolved with a Gaussian, and fitting functions for both correlated and uncorrelated backgrounds. The two Gaussian functions are used to fit the ω and ϕ mesons, while the Breit-Wigner convolved with a Gaussian is used to fit the ρ meson. The fit parameters are fixed to the world average values for the masses of the three vector mesons [39] while the widths of the Gaussian distributions account

for the detector mass resolution and are constrained by the values obtained from simulation. Because the invariant mass peaks of ω and ρ mesons cannot be resolved, the combined yield of these two mesons is extracted. The ratio of the ω and ρ mesons, N_ρ/N_ω , is set to 0.58, derived as the ratio of their corresponding production cross sections, $\sigma_\rho/\sigma_\omega = 1.15 \pm 0.15$, consistent with values found in jet fragmentation [24], multiplied by the ratio of their branching ratios [30, 39].

To describe the uncorrelated background in the unlike-sign invariant mass spectrum, the mixed-event distribution is fitted with a modified Hagedorn function [40–42]:

$$\frac{d^2N}{dm_{\mu\mu}dp_T} = \frac{p_0}{[\exp(-p_1m_{\mu\mu} - p_2m_{\mu\mu}^2) + m_{\mu\mu}/p_3]^{p_4}}, \quad (1)$$

where $m_{\mu\mu}$ is the reconstructed dimuon mass, p_0 is a normalization parameter, p_4 is the high mass tail parameter, and p_1 , p_2 , and p_3 are additional fit parameters. To assess the stability of the modified Hagedorn fit, the mixed-event distribution was fitted by a polynomial of 4th order and a modified Hagedorn function is used to fit the unlike-sign dimuon spectrum in the nonresonance region. The results of all three fits were consistent within uncertainties and the variations are taken as a systematic uncertainty on the yield extraction. The correlated background is well described by the function in Eq. 1,

$$f(m_{\mu\mu}) = a \exp(bm_{\mu\mu}), \quad (2)$$

where a and b are free parameters of the fit $f(m_{\mu\mu})$.

Each rapidity region ($1.2 < |y| < 2.2$) in the $p+p$ data set is sorted into the following p_T bins: [2.5, 3.0], [3.0, 3.5], and [3.5, 6.0] GeV/c. Figure 3 shows the results of fitting the dimuon spectra for each of these p_T bins. The fit function in Fig. 3 does not adequately capture the $\omega + \rho$ signal peak. As a result, the unlike-sign spectra were integrated over the $\omega + \rho$ and ϕ signal regions after subtracting the total background fit function to obtain the raw yields. The integral and fit values were consistent for the ϕ meson, while for $\omega + \rho$ mesons, the fit values were up to 8% lower than the integral values in some cases. Therefore, the integral values were adopted.

In the Au+Au data set, the statistics are insufficient to sort the data into p_T or centrality bins for each arm individually. However, due to the symmetry of the Au+Au collisions, the invariant yields for each arm are found to be consistent, with the means and widths of the fits for both ϕ and $\omega + \rho$ mesons being consistent between arms. Therefore, the raw yield as a function of p_T and as a function of centrality can be extracted for the combined sum of the north and south arms. Because the north and south arms have different $A\varepsilon$ values, as shown in Fig. 2, a simple sum cannot be used. Instead, the north arm is scaled by $A\varepsilon_{\text{south}}/A\varepsilon_{\text{north}}$, as a function of p_T and centrality, before being added to the south arm. The resulting yields are then weighted by $A\varepsilon_{\text{south}}$ when calculating the invariant yield.

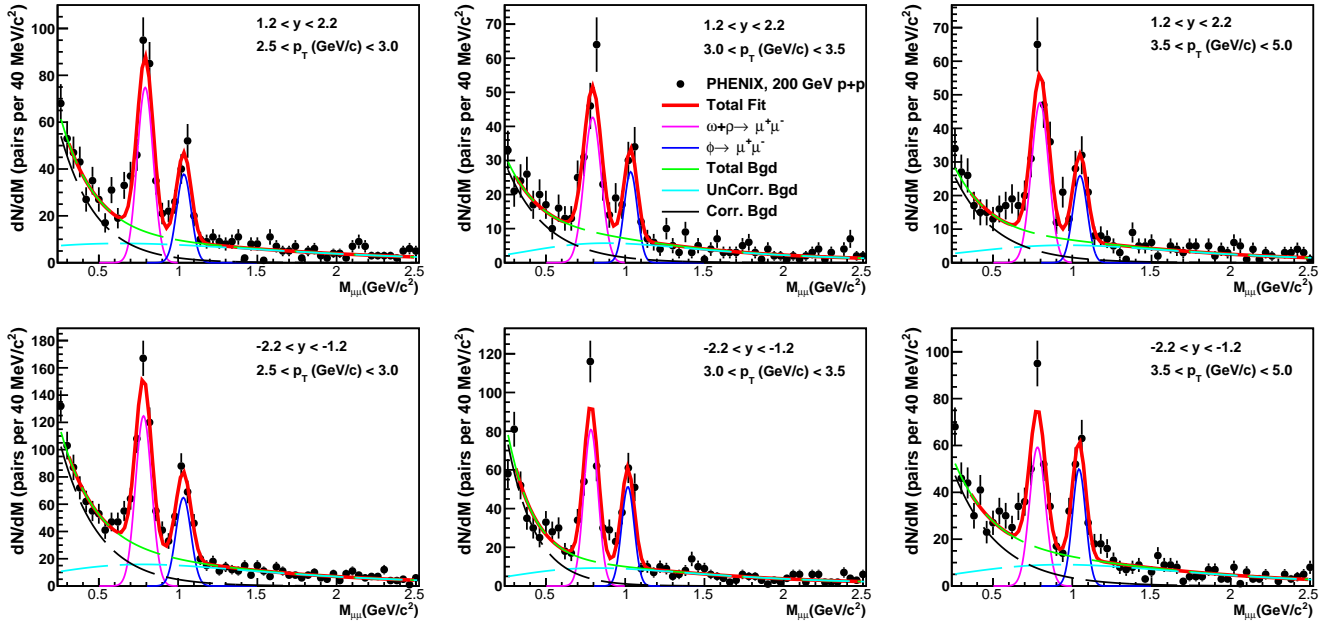


FIG. 3. The fitted raw unlike-sign dimuon spectra (black points) in $p+p$ collisions are shown for the different p_T bins at forward (top) and backward (bottom) rapidities. The panels also show the fits for the uncorrelated background (dashed cyan), correlated background (dashed black), $\omega + \rho$ mesons (solid magenta), ϕ meson (solid blue), and the total fit (solid red).

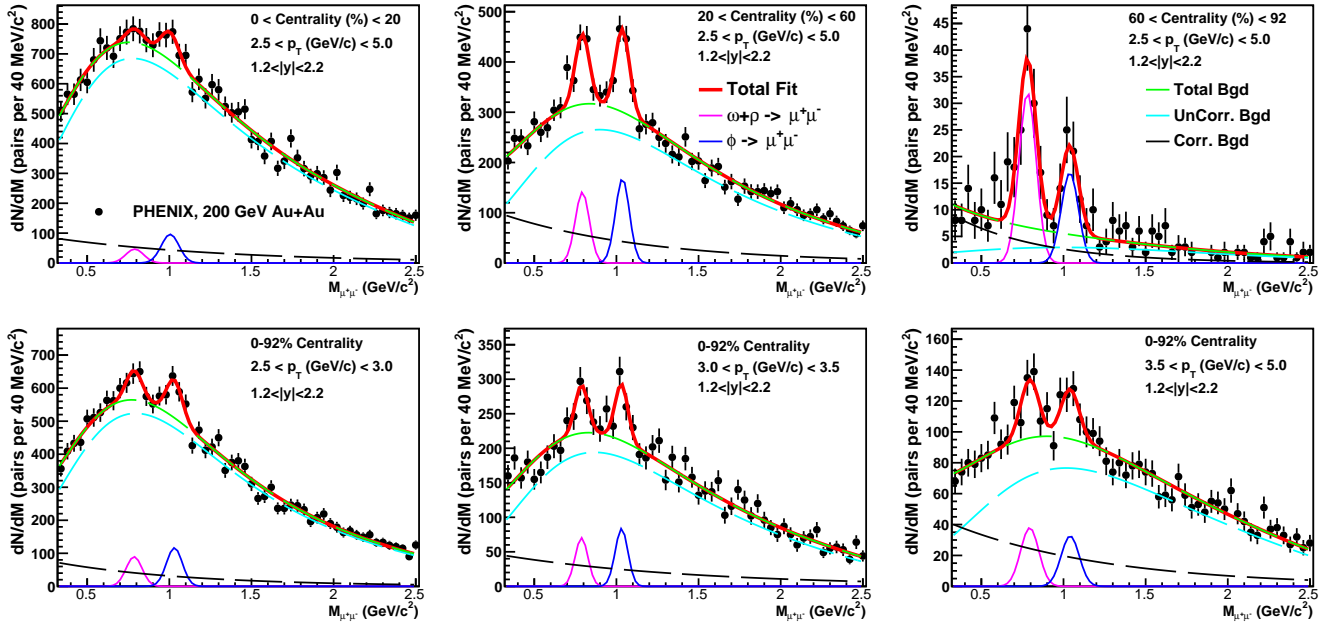


FIG. 4. The fitted raw unlike-sign dimuon spectra (black points) in Au+Au collisions are shown for different centrality classes (top) and p_T bins (bottom). The panels also show the fits for the uncorrelated background (dashed cyan), correlated background (dashed black), $\omega + \rho$ mesons (solid magenta), ϕ meson (solid blue), and the total fit (solid red).

Similar to the $p+p$ data set, the p_T distribution in the Au+Au data set is sorted into the following bins: $[2.5, 3.0]$, $[3.0, 3.5]$, and $[3.5, 6.0]$ GeV/c, while the centrality distribution is sorted into the bins: $[0, 20]$, $[20, 60]$, and $[60, 92]$. Figure 4 shows the results of fitting the dimuon

spectra for different centrality and p_T bins in case of the Au+Au data set. The fits in this figure include a modified Hagedorn to describe the uncorrelated background. As discussed earlier, two additional descriptions are used in extracting the LVM yields. The LVM yields were consis-

tent among all three fits within the uncertainties. Therefore, the best estimate for the invariant yield is taken as the RMS of all the fit methods, with its uncertainty calculated as the RMS of their individual uncertainties. The variations are considered as the systematic uncertainty for the yield extraction.

D. Calculation of invariant yields and nuclear-modification factors

The dimuon LVM invariant yield in a given p_T and centrality bin is

$$\frac{B_{\mu\mu}}{2\pi p_T} \frac{d^2 N}{dy dp_T} = \frac{1}{2\pi p_T} \frac{1}{\Delta y \Delta p_T} \frac{N_{\omega+\rho(\phi)}}{A\epsilon N_{\text{evt}}}, \quad (3)$$

where $B_{\mu\mu}$ is the branching ratio to dimuons, $N_{\omega+\rho(\phi)}$ is the number of observed mesons, N_{evt} is the number of MB events sampled in the given centrality bin, Δy is the width of the rapidity bin, and Δp_T is the width of the p_T bin. $A\epsilon$ is the acceptance and reconstruction efficiency. In $p+p$ collisions, the differential cross section, $d^2\sigma/dy dp_T$, is evaluated according to the following relation:

$$\frac{d^2\sigma}{dy dp_T} = \frac{d^2 N}{dy dp_T} \sigma_{\text{tot}}, \quad (4)$$

where $\sigma_{\text{tot}} = \sigma_{\text{BBC}}/\epsilon_{\text{MB}}^{\text{BBC}}$ is the total cross section. σ_{BBC} is the BBC cross section, 23.0 ± 2.2 mb at $\sqrt{s} = 200$ GeV, which is determined from the van der Meer scan technique, and $\epsilon_{\text{MB}}^{\text{BBC}}$ is MB trigger efficiency, 0.545 [43].

To gain insight into nuclear medium effects and particle production mechanisms in Au+Au collisions, the ratio of the LVM yields in Au+Au collisions to $p+p$ collisions scaled by $\langle N_{\text{coll}} \rangle$ for that centrality bin in the Au+Au system [44], is calculated as

$$R_{AA} = \frac{d^2 N_{AA}/dy dp_T}{\langle N_{\text{coll}} \rangle \times d^2 N_{pp}/dy dp_T}, \quad (5)$$

where R_{AA} is the nuclear-modification factor, $d^2 N_{AA}/dy dp_T$ is the per-event yield of particle production in Au+Au collisions and $d^2 N_{pp}/dy dp_T$ is the per event yield of the same process in $p+p$ collisions [30].

E. Systematic uncertainties

The systematic uncertainties are categorized into three types according to their impact on the measured results. All uncertainties are expressed as one standard deviation.

Type-A: point-to-point uncorrelated uncertainties, meaning that the data points can vary independently of each other. These uncertainties are combined in quadrature with statistical uncertainties. To account for the

variation in yield when different functions are used to fit the uncorrelated background, a 6% uncertainty is assigned in signal extraction for the Au+Au data set and for the $p+p$ data set a 5.0% (4.5%) uncertainty is assigned for the north (south) arm.

Type-B: point-to-point correlated uncertainties which allow the data points to move coherently within the quoted range to some degree. These systematic uncertainties include a 4% uncertainty from MuID tube efficiency and a 2% from MuTr overall efficiency. Furthermore, the systematic uncertainty in $A\epsilon$ due to the input p_T is 6.3%. In the case of the Au+Au data set, the systematic uncertainties related to the azimuthal distribution of the muon tracks are 10.4% for the north arm and 6.7% for the south arm. Because invariant yields and nuclear modification factors are calculated by adding the north and south arms, the azimuthal distribution uncertainties are added in quadrature, resulting in a total uncertainty of 12.4%. In the case of the $p+p$ data, the systematic uncertainty related to the azimuthal distribution of the muon tracks is 7.5% (6.4%) for the north (south) arm. The Type-B systematic uncertainties are added in quadrature. For the Au+Au dataset, these uncertainties total 14.6%. In the case of the $p+p$ dataset, they amount to 10.3% for the north arm and 9.6% for the south arm. These uncertainties are shown as boxes around the data points.

Type-C: an overall normalization uncertainty of 10% for $p+p$ is assigned to the BBC bias correction uncertainties [45]. No correction is applied for Au+Au collisions. All systematic uncertainties included in the invariant calculations are summarized in Table I.

TABLE I. Systematic uncertainties included in the invariant yield calculations.

Type	Origin	Au+Au	$p+p$ north (south)
A	Signal extraction	6%	5% (4.5%)
B	MuID hit efficiency	4%	4%
B	MuTr hit efficiency	2%	2%
B	$A\epsilon$ p_T	6.3%	5.5%
B	$A\epsilon$ φ distribution	12.4%	7.5% (6.4%)
B	Quadratic sum	14.6%	10.3% (9.6%)
C	MB trigger efficiency	–	10%

For the nuclear-modification factor, the type-A systematic uncertainties are included in the statistical uncertainties of the Au+Au and $p+p$ invariant yields, as mentioned earlier. The systematic uncertainties that include MuID and MuTr efficiencies are the same between the invariant yields of Au+Au and $p+p$ and cancel out. A 9.3% (8.4%) systematic uncertainty in $A\epsilon$ for the north (south) arm, which is carried over from $p+p$, is added in quadrature to the type-B systematic uncertainties listed in Table I. Type-C systematic uncertainties for R_{AA} are calculated as the quadratic sum of the Type-C system-

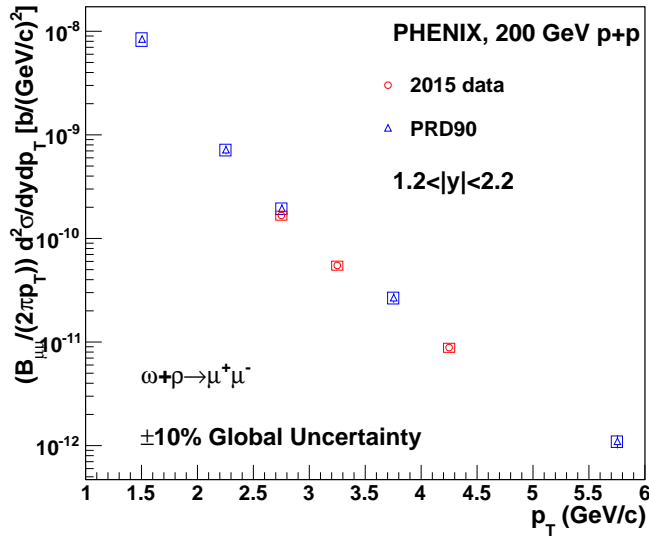


FIG. 5. The differential cross sections of $\omega + \rho$ mesons as a function of p_T in $p+p$ collisions for the data sets collected in 2015 (empty red circles) and 2009 (empty blue triangles) [30]. The systematic uncertainties of type-A are combined with statistical uncertainties in quadrature and are represented as error bars. Type-B systematic uncertainties are displayed as boxes around the data points.

atic uncertainties from the $p+p$ collisions and the uncertainty in $\langle N_{\text{coll}} \rangle$. The latter contributes an uncertainty of 9%, based on the Glauber model calculations for Au+Au collisions averaged over all centralities. However, when R_{AA} is presented as a function of $\langle N_{\text{part}} \rangle$, the uncertainty associated with $\langle N_{\text{coll}} \rangle$ is instead included as a Type-B uncertainty, summed in quadrature with other Type-B contributions.

IV. RESULTS

The differential cross sections of $\omega + \rho$ and ϕ mesons as a function of p_T in $p+p$ collisions at $\sqrt{s} = 200$ GeV are presented in Figs. 5 and 6, respectively. Both figures show comparisons between previously published PHENIX data [30] and current measurements from the data collected in 2015, and they are consistent within uncertainties. The invariant yields of $\omega + \rho$ and ϕ mesons in $p+p$ collisions at $\sqrt{s} = 200$ GeV, obtained from the data collected in 2015, serve as a reference for the measurements of the nuclear-modification factor.

Figures 7 and 8 show the LVM invariant yields in Au+Au as a function of p_T , integrated over 0%–92% centrality, and as a function of the average number of participating nucleons ($\langle N_{\text{part}} \rangle$), respectively. The ϕ meson distribution is softer compared to the $\omega + \rho$ mesons distribution within the studied p_T range, and its yield is lower than the $\omega + \rho$ yield in the most peripheral collisions.

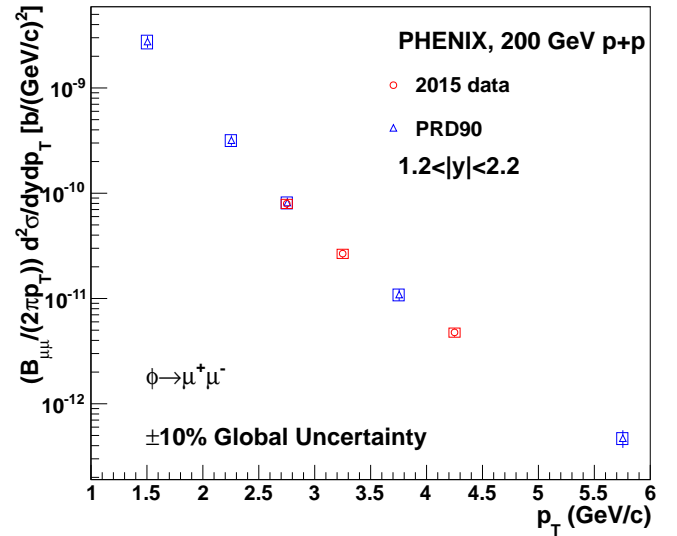


FIG. 6. The differential cross sections of ϕ meson as a function of p_T in $p+p$ collisions for the data sets collected in 2015 (empty red circles) and 2009 (empty blue triangles) [30]. The systematic uncertainties of type-A are combined with statistical uncertainties in quadrature and are represented as error bars. Type-B systematic uncertainties are displayed as boxes around the data points.

Figure 9 shows the R_{AA} for the ϕ meson in Au+Au collisions integrated over all centralities as a function of p_T , measured over the rapidity range $1.2 < |y| < 2.2$. The R_{AA} shows a hint of enhancement at intermediate p_T , though it remains consistent with unity within uncertainties, and exhibits significant suppression at higher p_T . Additionally, Fig. 9 shows the R_{AA} for the ϕ meson in Cu+Au collisions, measured across all centralities and at the same rapidity [38]. The Au-going result is consistent with this measurement within uncertainties. Similar nuclear modification pattern was observed at midrapidity [47].

Figure 10 shows the R_{AA} for the ϕ meson as a function of $\langle N_{\text{part}} \rangle$ in Au+Au collisions measured over the p_T range $2.5 < p_T < 5.0$ GeV/c and in the rapidity region $1.2 < |y| < 2.2$. The R_{AA} exhibits an enhancement around intermediate $\langle N_{\text{part}} \rangle \approx 100$, while remaining largely unchanged elsewhere. These results agree within uncertainties with the PHENIX measurements at midrapidity [18] for both Au+Au and Cu+Au collisions. While the midrapidity data hints at a possible enhancement at lower $\langle N_{\text{part}} \rangle$, ≈ 50 , which is likely due to the lower p_T range covered ($2 < p_T < 5$ GeV/c). Nevertheless, this enhancement remains consistent with unity when considering the uncertainties. Additionally, Fig. 10 shows the ALICE R_{AA} of the ϕ in Pb+Pb collisions at 2.76 TeV over a similar p_T range, $2 < p_T < 5$ GeV/c, but at more forward rapidity, $2.5 < y < 4$ [46]. Although both this and the ALICE measurements have considerable uncertainties, this result clearly shows an enhance-

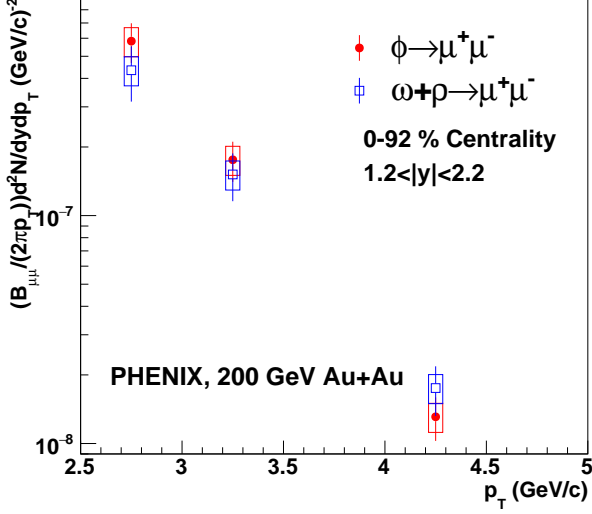


FIG. 7. The invariant yields of ϕ (solid red circles) and $\omega + \rho$ (empty blue squares) mesons as a function of p_T in Au+Au collisions. The systematic uncertainties of type-A are combined with statistical uncertainties in quadrature and are represented as error bars. Type-B systematic uncertainties are displayed as boxes around the data points.

ment at intermediate $\langle N_{\text{part}} \rangle$, while the ALICE measurement shows no enhancement. This could suggest an energy dependence of strangeness enhancement at forward rapidity.

The R_{AA} of the $\omega + \rho$ mesons in Au+Au collisions summed for all centralities as a function of p_T , measured over the rapidity range $1.2 < |y| < 2.2$, is shown in Fig. 11, which also shows the ω and π^0 mesons R_{AA} at midrapidity [48, 49]. The $\omega + \rho$ mesons show a similar suppression to that of the ω meson at midrapidity. It should be noted that this measurement, which measures the sum of the ω and ρ mesons, is consistent with the ω meson only, suggesting that the ω and ρ mesons exhibit similar suppression patterns.

The R_{AA} of the $\omega + \rho$ mesons as a function of the average number of participants is shown in Fig. 12. In peripheral collisions, R_{AA} is consistent with unity within uncertainties, indicating no nuclear modification. In the most central and intermediate collisions, R_{AA} is reduced to approximately 0.3 and 0.6, respectively, showing strong suppression in the most central collisions and moderate suppression in intermediate collisions, relative to the $p+p$ reference.

Although the PHENIX midrapidity measurement [48] extends p_T coverage down to 0.3 GeV/c, the results remain consistent with the current measurement. Figure 12 also includes the R_{AA} for the π^0 meson at midrapidity [48, 49]. Although the π^0 meson R_{AA} exhibits a suppression pattern similar to that of the $\omega + \rho$ mesons in intermediate and central collisions, the suppression persists even in the most peripheral collisions.

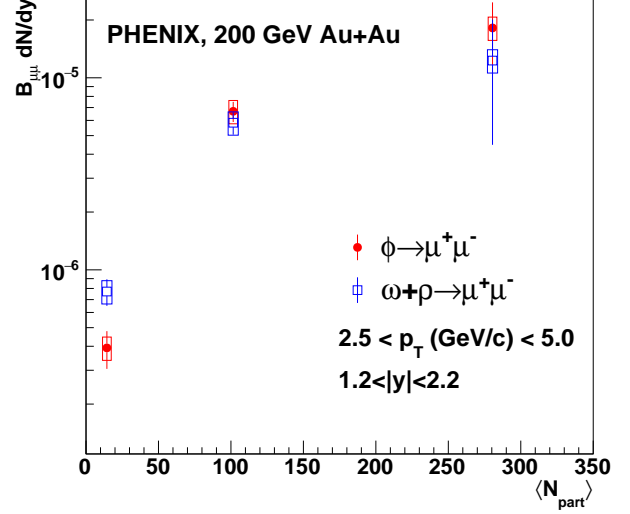


FIG. 8. The invariant yields of ϕ (solid red circles) and $\omega + \rho$ (empty blue squares) mesons as a function of $\langle N_{\text{part}} \rangle$ in Au+Au collisions. The systematic uncertainties of type-A are combined with statistical uncertainties in quadrature and are represented as error bars. Type-B systematic uncertainties are displayed as boxes around the data points.

Figure 13 presents the R_{AA} of the $\omega + \rho$, ϕ , and J/ψ mesons as a function of p_T in the rapidity regions $1.2 < |y| < 2.2$ in Au+Au collisions at $\sqrt{s_{NN}} = 200$ GeV [29]. This comparison allows for the investigation of flavor dependence in medium effects within systems containing light, strange, and charm quarks, specifically in the $\omega + \rho$, ϕ , and J/ψ mesons. The $\omega + \rho$ mesons, representing the light flavor, exhibit the most pronounced suppression over the covered p_T range. In contrast, the ϕ meson, representing the strange flavor, displays a more complex pattern. It shows no suppression, maybe a hint of enhancement, in the intermediate p_T range, followed by a suppression at higher p_T values that is comparable to light flavor. The J/ψ meson, representing the heavy flavor, demonstrates suppression across the full covered p_T range, extending even to very low p_T values. However, its suppression pattern differs from that of the light flavor. The J/ψ suppression is more pronounced at low p_T and becomes less severe as p_T increases.

A comparison similar to that shown in Fig. 13 is presented in Fig. 14, but this time as a function of $\langle N_{\text{part}} \rangle$. In the most central collisions, the $\omega + \rho$ and J/ψ mesons exhibit suppression, while the ϕ meson remains largely unchanged. At intermediate centralities (around $\langle N_{\text{part}} \rangle \approx 100$), $\omega + \rho$ and J/ψ mesons show similar moderate suppression, while the ϕ meson has large R_{AA} . In peripheral collisions, $\omega + \rho$ mesons deviate from the trend observed for the J/ψ meson and show no nuclear modification, behaving similarly to the ϕ meson in this region.

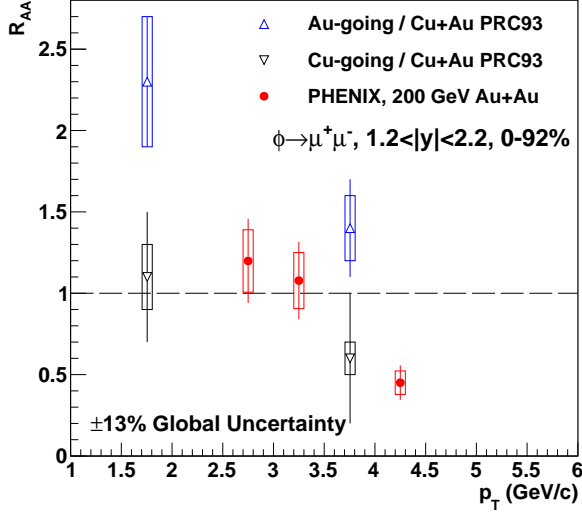


FIG. 9. The R_{AA} of ϕ meson as a function of p_T for $1.2 < |y| < 2.2$ in Au+Au collisions at $\sqrt{s_{NN}} = 200$ GeV, compared with Cu+Au collisions [38]. The systematic uncertainties of type-A are combined with statistical uncertainties in quadrature and are displayed as error bars. Type-B systematic uncertainties are shown as boxes around the data points.

V. SUMMARY

We have measured the production of $\omega + \rho$ and ϕ mesons at forward and backward rapidities via the $\mu^+\mu^-$ decay channel in $p+p$ and Au+Au collisions at $\sqrt{s_{NN}} = 200$ GeV. This study represents the first measurement of the invariant yields and nuclear-modification factors for $\omega + \rho$ and ϕ mesons in Au+Au collisions at RHIC in the forward/backward rapidity regions. The results are presented as a function of $\langle N_{part} \rangle$ and p_T .

In Au+Au collisions, the R_{AA} for the ϕ meson shows strong suppression at higher p_T , while remaining consistent with unity at low to intermediate p_T within uncertainties. This behavior is consistent with previous findings from Cu+Au collisions [38]. Furthermore, the R_{AA} of the ϕ meson as a function of $\langle N_{part} \rangle$ reveals distinct trends. An enhancement is observed at intermediate $\langle N_{part} \rangle$, while it remains largely unchanged at other values. These observations are consistent with PHENIX measurements at midrapidity within experimental uncertainties. Additionally, measurements by ALICE at the LHC [46] show no enhancement across all centralities.

In the measured region, the $\omega + \rho$ mesons exhibits a suppression pattern similar to that of the ω meson as a function of p_T and $\langle N_{part} \rangle$. In addition, within uncertainties, these results are also consistent with those observed for the π^0 meson. However, it is worth noting that the π^0 meson consistently shows a more pronounced suppression. The observed similarity in suppression between $\omega + \rho$ and ω mesons suggests that the ρ meson may

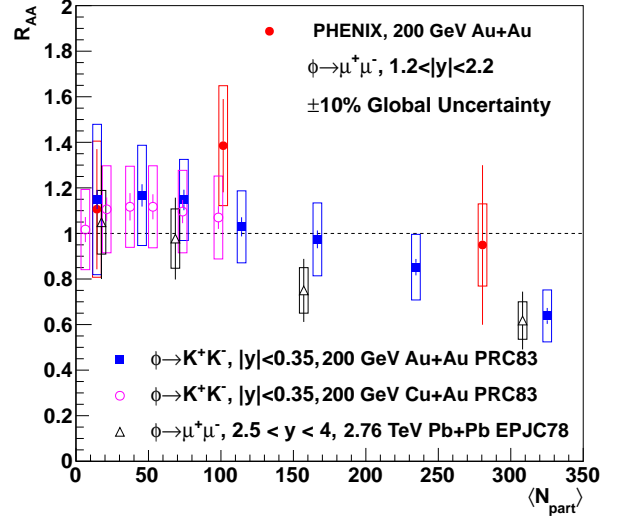


FIG. 10. The R_{AA} of ϕ meson as a function of $\langle N_{part} \rangle$ for $1.2 < |y| < 2.2$ in Au+Au collisions at $\sqrt{s_{NN}} = 200$ GeV, compared with the PHENIX measurements at $|y| < 0.35$ in Au+Au and Cu+Au collisions at $\sqrt{s_{NN}} = 200$ GeV [18]. Results at the LHC from ALICE at $2.5 < y < 4$ in Pb+Pb collisions at 2.76 TeV are also shown for comparison [46].

exhibit a similar suppression pattern to the ω meson.

The flavor dependence of medium effects is examined by comparing the R_{AA} of the ϕ , $\omega + \rho$, and J/ψ mesons. Both $\omega + \rho$ and J/ψ mesons exhibit suppression across the entire p_T range, though their p_T dependence differs slightly. Their behavior as a function of $\langle N_{part} \rangle$ is generally similar, except in peripheral collisions where they diverge. In contrast, the strange flavor (ϕ meson) shows a distinct pattern, with enhancement observed at intermediate values of both p_T and $\langle N_{part} \rangle$.

In conclusion, the analysis provides valuable information on the production and nuclear modification of $\omega + \rho$ and ϕ mesons in heavy-ion collisions, with both mesons showing significant nuclear medium effects, especially at higher p_T and central collisions. These results on low-mass vector meson production in relativistic heavy-ion collisions contribute to the understanding of particle production and the behavior of nuclear matter in extreme conditions.

ACKNOWLEDGMENTS

We thank the staff of the Collider-Accelerator and Physics Departments at Brookhaven National Laboratory and the staff of the other PHENIX participating institutions for their vital contributions. We acknowledge support from the Office of Nuclear Physics in the Office of Science of the Department of Energy, the National Science Foundation, Abilene Christian University

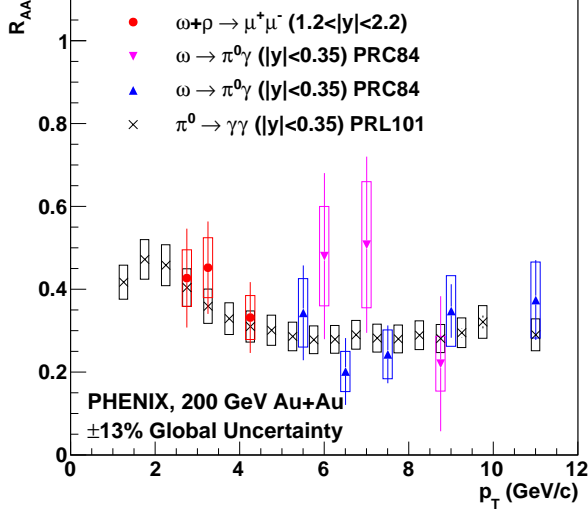


FIG. 11. R_{AA} of $\omega + \rho$ mesons as a function of p_T at $1.2 < |y| < 2.2$ in Au+Au collisions at $\sqrt{s_{NN}} = 200$ GeV (red points), compared with PHENIX ω measurements at $|y| < 0.35$ (blue and inverted magenta triangles) [48] and π^0 (black stars) [49].

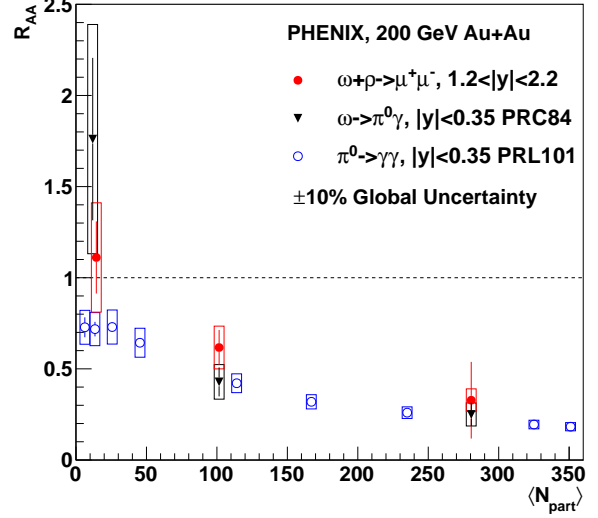


FIG. 12. R_{AA} of $\omega + \rho$ mesons as a function of $\langle N_{part} \rangle$ in Au+Au collisions, obtained from the dimuon decay channel (solid red points), is compared with R_{AA} of ω at midrapidity obtained from the $\pi^0 \gamma$ decay channel (inverted black triangles) [48]. Additionally, the results for R_{AA} of π^0 are shown (empty blue circles) for comparison [49].

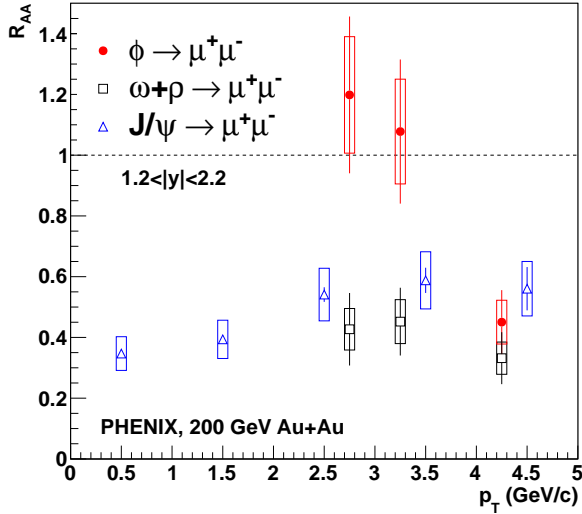


FIG. 13. Comparison of R_{AA} as a function of p_T for ϕ (solid [red] circles), $\omega + \rho$ (empty [black] squares), and J/ψ (empty [blue] triangles) in mesons Au+Au collisions at $\sqrt{s_{NN}} = 200$ GeV [29].

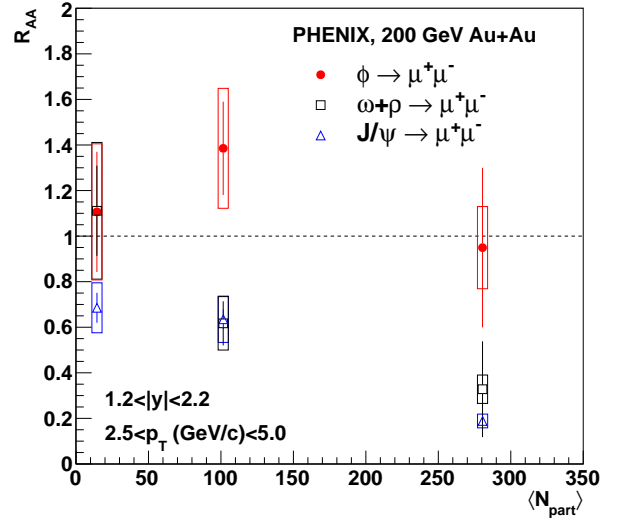


FIG. 14. Comparison of R_{AA} as a function of $\langle N_{part} \rangle$ for ϕ (solid [red] circles), $\omega + \rho$ (open [black] squares), and J/ψ mesons (open [blue] triangles) in Au+Au collisions at $\sqrt{s_{NN}} = 200$ GeV [29].

Research Council, Research Foundation of SUNY, and Dean of the College of Arts and Sciences, Vanderbilt University (U.S.A), Ministry of Education, Culture, Sports, Science, and Technology and the Japan Society for the Promotion of Science (Japan), Conselho Nacional de Desenvolvimento Científico e Tecnológico and Fundação de Amparo à Pesquisa do Estado de São Paulo (Brazil),

Natural Science Foundation of China (People's Republic of China), Croatian Science Foundation and Ministry of Science and Education (Croatia), Ministry of Education, Youth and Sports (Czech Republic), Centre National de la Recherche Scientifique, Commissariat à l'Énergie Atomique, and Institut National de Physique Nucléaire et de Physique des Particules (France), Bundesminis-

terium für Bildung und Forschung, Deutscher Akademischer Austausch Dienst, and Alexander von Humboldt Stiftung (Germany), J. Bolyai Research Scholarship, EFOP, HUN-REN ATOMKI, NKFIH, MATE KKF, and OTKA (Hungary), Department of Atomic Energy and Department of Science and Technology (India), Israel Science Foundation (Israel), Basic Science Research and SRC(CENuM) Programs through NRF funded by the Ministry of Education and the Ministry of Science and

ICT (Korea). Ministry of Education and Science, Russian Academy of Sciences, Federal Agency of Atomic Energy (Russia), VR and Wallenberg Foundation (Sweden), University of Zambia, the Government of the Republic of Zambia (Zambia), the U.S. Civilian Research and Development Foundation for the Independent States of the Former Soviet Union, the Hungarian American Enterprise Scholarship Fund, the US-Hungarian Fulbright Foundation, and the US-Israel Binational Science Foundation.

-
- [1] K. Adcox *et al.* (PHENIX Collaboration), Formation of dense partonic matter in relativistic nucleus-nucleus collisions at RHIC: Experimental evaluation by the PHENIX collaboration, Nucl. Phys. A **757**, 184 (2005).
 - [2] I. Arsene *et al.*, Quark-gluon plasma and color glass condensate at RHIC? The perspective from the BRAHMS experiment, Nucl. Phys. A **757**, 1 (2005), first Three Years of Operation of RHIC.
 - [3] B. Back *et al.*, The PHOBOS perspective on discoveries at RHIC, Nucl. Phys. A **757**, 28 (2005), first Three Years of Operation of RHIC.
 - [4] J. Adams *et al.*, Experimental and theoretical challenges in the search for the quark-gluon plasma: The STAR Collaboration's critical assessment of the evidence from RHIC collisions, Nucl. Phys. A **757**, 102 (2005), first Three Years of Operation of RHIC.
 - [5] S. Chatrchyan *et al.*, Study of high- p_T charged particle suppression in PbPb compared to pp collisions at $\sqrt{s_{NN}}=2.76$ TeV, The European Physical Journal C **72**, 1945 (2012).
 - [6] B. Abelev *et al.*, Centrality dependence of charged particle production at large transverse momentum in Pb-Pb collisions at $\sqrt{s_{NN}}=2.76$ TeV, Phys. Lett. B **720**, 52 (2013).
 - [7] G. Aad *et al.*, Measurement of the jet radius and transverse momentum dependence of inclusive jet suppression in lead-lead collisions at $\sqrt{s_{NN}} = 2.76$ TeV with the ATLAS detector, Phys. Lett. B **719**, 220 (2013).
 - [8] T. Gunji, Overview of recent ALICE results, Nucl. Phys. A **956**, 11 (2016), the XXV International Conference on Ultrarelativistic Nucleus-Nucleus Collisions: Quark Matter 2015.
 - [9] P. Koch, B. Mueller, and J. Rafelski, Strangeness in relativistic heavy ion collisions, Phys. Reports **142**, 167 (1986).
 - [10] A. Shor, ϕ -Meson Production as a Probe of the Quark-Gluon Plasma, Phys. Rev. Lett. **54**, 1122 (1985).
 - [11] B. Alessandro *et al.*, ϕ production in Pb-Pb collisions at 158 GeV/c per nucleon incident momentum, Phys. Lett. B **555**, 147 (2003).
 - [12] S. S. Adler *et al.* (PHENIX Collaboration), Production of phi mesons at midrapidity in $\sqrt{s_{NN}} = 200$ GeV Au+Au collisions at RHIC, Phys. Rev. C **72**, 014903 (2005), arXiv:nucl-ex/0410012.
 - [13] S. Afanasiev *et al.* (PHENIX Collaboration), Elliptic Flow for ϕ Mesons and (Anti)deuterons in Au+Au Collisions at $\sqrt{s_{NN}} = 200$ GeV, Phys. Rev. Lett. **99**, 052301 (2007).
 - [14] B. I. Abelev *et al.* (STAR Collaboration), Partonic Flow and ϕ -Meson Production in Au + Au Collisions at $\sqrt{s_{NN}} = 200$ GeV, Phys. Rev. Lett. **99**, 112301 (2007).
 - [15] D. Adamova *et al.* (CERES Collaboration), Modification of the rho-meson detected by low-mass electron-positron pairs in central Pb-Au collisions at 158-A-GeV/c, Phys. Lett. B **666**, 425 (2008), arXiv:nucl-ex/0611022.
 - [16] C. Alt *et al.* (NA49 Collaboration), Energy dependence of ϕ meson production in central Pb + Pb collisions at $\sqrt{s_{NN}} = 6$ to 17 GeV, Phys. Rev. C **78**, 044907 (2008).
 - [17] B. Abelev *et al.*, Energy and system size dependence of ϕ meson production in Cu+Cu and Au+Au collisions, Phys. Lett. B **673**, 183 (2009).
 - [18] A. Adare *et al.* (PHENIX), Nuclear modification factors of ϕ mesons in d +Au, Cu+Cu and Au+Au collisions at $\sqrt{s_{NN}}=200$ GeV, Phys. Rev. C **83**, 024909 (2011), arXiv:1004.3532 [nucl-ex].
 - [19] R. Arnaldi *et al.*, A comparative measurement of $\phi \rightarrow K^+ + K^-$ and $\phi \rightarrow \mu^+ + \mu^-$ in In-In collisions at the CERN SPS, Phys. Lett. B **699**, 325 (2011).
 - [20] J. Rafelski and B. Müller, Strangeness Production in the Quark-Gluon Plasma, Phys. Rev. Lett. **48**, 1066 (1982).
 - [21] F. Rennecke, W. jie Fu, and J. M. Pawlowski, Strangeness neutrality and the QCD phase diagram (2019), arXiv:1907.08179 [hep-ph].
 - [22] W. Dai *et al.*, Nuclear suppression of the ϕ meson yields with large at the RHIC and the LHC. , Eur. Phys. J. C **77**, 571 (2017).
 - [23] U. Acharya *et al.* (PHENIX), Study of ϕ -meson production in p +Al, p +Au, d +Au, and ^3He +Au collisions at $\sqrt{s_{NN}} = 200$ GeV, Phys. Rev. C **106**, 014908 (2022), arXiv:2203.06087 [nucl-ex].
 - [24] W.-M. Yao *et al.*, Rev. Part. Phys., J. Phys. G **33**, 1 (2006).
 - [25] X.-N. Wang, Why the observed jet quenching at RHIC is due to parton energy loss, Phys. Lett. B **579**, 299 (2004).
 - [26] H. van Hees and R. Rapp, Dilepton radiation at the CERN super-proton synchrotron, Nucl. Phys. A **806**, 339 (2008).
 - [27] C. A. Dominguez, M. Loewe, and Y. Zhang, Chiral symmetry restoration and deconfinement in QCD at finite temperature, Phys. Rev. D **86**, 034030 (2012).
 - [28] P. Petreczky, Lattice QCD at non-zero temperature, J. Phys. G **39**, 093002 (2012).
 - [29] A. Adare *et al.* (PHENIX Collaboration), J/ψ Production versus Centrality, Transverse Momentum, and Rapidity in Au + Au Collisions at $\sqrt{s_{NN}} = 200$ GeV, Phys. Rev. Lett. **98**, 232301 (2007).

- [30] A. Adare *et al.* (PHENIX Collaboration), Low-mass vector-meson production at forward rapidity in $p+p$ collisions at $\sqrt{s} = 200$ GeV, Phys. Rev. D **90**, 052002 (2014).
- [31] K. Adcox, *et al.*, PHENIX detector overview, Nucl. Instrum. Methods Phys. Res., Sec. A **499**, 469 (2003), the Relativistic Heavy Ion Collider Project: RHIC and its Detectors.
- [32] C. Aidala *et al.*, The PHENIX Forward Silicon Vertex Detector, Nucl. Instrum. Methods Phys. Res., Sec. A **755**, 44 (2014).
- [33] H. Akikawa *et al.*, PHENIX Muon Arms, Nucl. Instrum. Methods Phys. Res., Sec. A **499**, 537 (2003), the Relativistic Heavy Ion Collider Project: RHIC and its Detectors.
- [34] A. Adare *et al.* (PHENIX Collaboration), J/ψ suppression at forward rapidity in Au + Au collisions at $\sqrt{s_{NN}} = 200$ GeV, Phys. Rev. C **84**, 054912 (2011).
- [35] A. Adare *et al.* (PHENIX Collaboration), Centrality categorization for $R_{p(d)+A}$ in high-energy collisions, Phys. Rev. C **90**, 034902 (2014).
- [36] T. Sjostrand, P. Eden, C. Friberg, L. Lonnblad, G. Miu, S. Mrenna, and E. Norrbin, High-energy physics event generation with PYTHIA 6.1, Comput. Phys. Commun. **135**, 238 (2001).
- [37] S. Agostinelli *et al.*, Geant4- a simulation toolkit, Nucl. Instrum. Methods Phys. Res., Sec. A **506**, 250 (2003).
- [38] A. Adare *et al.* (PHENIX Collaboration), ϕ meson production in the forward/backward rapidity region in Cu + Au collisions at $\sqrt{s_{NN}} = 200$ GeV, Phys. Rev. C **93**, 024904 (2016).
- [39] J. Beringer *et al.* (Particle Data Group), Rev. Part. Phys., Phys. Rev. D **86**, 010001 (2012).
- [40] A. Adare *et al.* (PHENIX Collaboration), Heavy-quark production in $p + p$ and energy loss and flow of heavy quarks in Au + Au collisions at $\sqrt{s_{NN}} = 200$ GeV, Phys. Rev. C **84**, 044905 (2011).
- [41] C. Aidala *et al.* (PHENIX Collaboration), Measurements of $\mu\mu$ pairs from open heavy flavor and Drell-Yan in $p+p$ collisions at $\sqrt{s} = 200$ GeV, Phys. Rev. D **99**, 072003 (2019).
- [42] U. Acharya *et al.* (PHENIX Collaboration), Measurement of J/ψ at forward and backward rapidity in $p + p$, $p + \text{Al}$, $p + \text{Au}$, and $^3\text{He} + \text{Au}$ collisions at $\sqrt{s_{NN}} = 200$ GeV, Phys. Rev. C **102**, 014902 (2020).
- [43] A. Adare *et al.* (PHENIX Collaboration), Inclusive cross section and double helicity asymmetry for π^0 production in $p + p$ collisions at $\sqrt{s} = 62.4$ GeV, Phys. Rev. D **79**, 012003 (2009).
- [44] S. S. Adler *et al.* (PHENIX Collaboration), Suppressed π^0 Production at Large Transverse Momentum in Central Au+Au Collisions at $\sqrt{s_{NN}} = 200$ GeV, Phys. Rev. Lett. **91**, 072301 (2003).
- [45] A. Adare *et al.* (PHENIX Collaboration), $\Upsilon(1s+2s+3s)$ production in $d+\text{Au}$ and $p + p$ collisions at $\sqrt{s_{NN}} = 200$ gev and cold-nuclear-matter effects, Phys. Rev. C **87**, 044909 (2013).
- [46] S. Acharya *et al.*, ϕ meson production at forward rapidity in Pb–Pb collisions at $\sqrt{s_{NN}} = 2.76$ TeV, Eur. Phys. J. C **78**, 559 (2018).
- [47] N. J. Abdulameer *et al.* (PHENIX Collaboration), Measurement of ϕ -meson production in Cu + Au collisions at $\sqrt{s_{NN}} = 200$ GeV and U + U collisions at $\sqrt{s_{NN}} = 193$ GeV, Phys. Rev. C **107**, 014907 (2023).
- [48] A. Adare *et al.* (PHENIX Collaboration), Production of ω mesons in $p + p$, $d + \text{Au}$, $\text{Cu} + \text{Cu}$, and $\text{Au} + \text{Au}$ collisions at $\sqrt{s_{NN}} = 200$ GeV, Phys. Rev. C **84**, 044902 (2011).
- [49] A. Adare *et al.* (PHENIX Collaboration), Suppression pattern of neutral pions at high transverse momentum in Au + Au collisions at $\sqrt{s_{NN}} = 200$ GeV and constraints on medium transport coefficients, Phys. Rev. Lett. **101**, 232301 (2008).